

AERODYNAMIC DESIGN AND ANALYSIS OF HLFC WINGS WITHIN THE EUROPEAN PROJECT HLFC-WIN

Thomas Streit¹, Martin Kruse², Thomas Kilian³, Judith v. Geyr⁴, Ilias Petropoulos⁵

¹ DLR, Lilienthalplatz 7, D-38108 Braunschweig, Germany, th.streit@dlr.de

² DLR, Lilienthalplatz 7, D-38108 Braunschweig, Germany, martin.kruse@dlr.de

³ DLR, Lilienthalplatz 7, D-38108 Braunschweig, Germany, Thomas.Kilian@dlr.de

⁴ DLR, Lilienthalplatz 7, D-38108 Braunschweig, Germany, judith.vgeyr@dlr.de

⁵ ONERA, 8 rue des Vertugadins, F-92190 Meudon, France, ilias.petropoulos@onera.fr

Abstract

Results for the numerical aerodynamic design and analysis of a long-range, large passenger aircraft equipped with a Hybrid Laminar Flow Control (HLFC) system are presented. This work was performed within the European project HLFC-WIN. The reference geometry of this study is the long-range cruise Airbus research XRF1 geometry, designed for turbulent flow. The HLFC part of the wing is restricted to an outer wing region which extends from the engine mounting to the wing tip. To achieve laminar flow in the outer wing, nose suction panels are used and the wing shape is changed. The aerodynamic HLFC wing design is performed at different cruise flight conditions. It involves shape design and optimization of the suction distribution. The shape design was performed using the DLR 3D transonic inverse design code. Results for the shape design are presented for three geometries. The first one is a DLR redesign of an HLFC variant of the XRF1 aircraft designed by Airbus. This geometry is used for the HLFC-WIN ground base demonstrator. Design was performed at the cruise design point and for off-design conditions. This design presents two improvements in comparison to the initial geometry: a) an increased laminar extent for the cruise design point and b) an increased spanwise thickness distribution, which leads to a thickness distribution comparable to the reference geometry. A second HLFC design was performed which improved the cruise design point aerodynamic performance of the first design, also by reducing wave drag. In a third design it was shown that in the region of the outermost suction panel a natural laminar flow (NLF) design was possible by using for the nose a crossflow attenuated NLF (CATNLF) strategy. The shape design was performed on simplified geometries. For final shape designs complete configuration CFD solutions were obtained using the TAU RANS solver of DLR. The aerodynamic performance of the different HLFC geometries was assessed by using the ffd72 far-field drag analysis software of ONERA for these solutions. In the shape design a generalized suction distribution based on the suction distribution of the Airbus HLFC design was used. After the shape design, the suction distribution was optimized for the GBD-DLR-2 design in order to minimize the suction power. A novel combined approach of variable porosity outer skin and suction chambers was introduced. In addition to the design and analysis of the HLFC geometries this work also describes extensions of the numerical methods used to predict the transition line position in the case of boundary layer suction. The physical representation of surface suction was improved by implementing and testing a direct suction boundary in the TAU solver.

Keywords: HLFC and NLF, transonic inverse design, far-field drag analysis, suction optimization, RANS suction boundary condition

1. Introduction

The environmental impact of civil aviation coupled with the growth of aircraft traffic have motivated the orientation of regulations towards restrictions for more fuel-efficient aircraft. To this end, the Advisory Council for Aviation Research and innovation in Europe (ACARE) has introduced stringent requirements aiming at a reduction of the environmental footprint of the aviation sector [1]. Goals of

the European Vision FlightPath 2050 address, among others, the reduction of pollutant emissions and perceived noise of flying aircraft, sustainability (alternative fuels, recycling) and atmospheric impact. Meanwhile, the “European Green Deal” has the ambitious target of zero net carbon emissions in aviation until 2050. To reduce aviation’s carbon footprint, kerosene alternatives such as sustainable aviation fuels (SAF), liquified hydrogen or electrification, are emerging, yet offer less energy density and are currently much more cost intensive in production, storage and operation [2]. Therefore, the decarbonization of aviation will be only possible if a large reduction of energy consumption is achieved. To achieve these ambitious objectives, improved aircraft components, and even disruptive technologies, must be developed both individually and collectively, with respect to their integration on the aircraft. Aerodynamic design methods can thus contribute to the reduction of pollutant emissions by the design of more fuel-efficient aircraft (i.e. reduced consumption for a given mission), in particular by reducing aerodynamic drag.

The subject of aerodynamic drag is however complex. Despite the existence of numerous approaches to drag reduction at a theoretical or elementary level, it is not often the case in terms of their application at an industrial level. Civil transport aircraft in particular make the integration of disruptive technologies difficult in practice, due to the need for manufacturing adaptations, design methodology validation, as well as cost, maintenance, certification and safety concerns. A promising way to achieve an important reduction of aerodynamic drag, under a reasonable increase of configuration complexity, is to delay transition in order to maintain a laminar flow over parts of the aircraft surface.

For long-range aircraft, which have wings with large leading edge sweep, the delay of transition of the flow from laminar to turbulent can be achieved by Hybrid Laminar Flow Control (HLFC) systems [3]-[4]. These couple the application of airfoil geometries adapted to natural laminar flow principles [5]-[6] with laminar flow control. Over the recent years, an evaluation of the impact of HLFC technology for large passenger aircraft is being carried out within the frame of the HLFC-WIN project, funded by the Clean Sky 2 Joint Undertaking under the European Union’s Horizon 2020 research and innovation programme. This programme is a research collaboration between Aernnova, DLR, ONERA and SONACA group, with Airbus as an industrial partner. In order to perform this assessment, an integral approach is followed, combining aerodynamic and structural studies, manufacturing, system design and integration (WIPS, Krueger flaps, suction system), wind-tunnel testing, small-scale demonstrators and a large-scale ground-based-demonstrator (GBD). These numerical and experimental studies are performed within a complete validation and verification process. In particular, this project aims at reaching a TRL4 (technology readiness level) on integrated component level for HLFC technology on transonic wings of mid- to long-haul transport aircraft.

The detailed design of a HLFC wing requires shape design and optimization of the suction distribution for the suction nose panels. Even if the aerodynamic design of transonic wings with laminar boundary layer has reached a large degree of maturity [7], obtaining a good HLFC design for a complete cruise configuration which shows acceptable laminar extent for the possible different cruise flight conditions is a challenge from the design and numerical point of view. The HLFC design presented here uses special pressure distributions. For the suction distribution, in order to fulfill the tight space requirements within an HLFC wing leading edge, a novel combined approach of variable-porosity outer skin and suction chambers was introduced. Although in HLFC-WIN the final evaluation of the HLFC configurations will be performed on an integral basis, i.e. including all disciplines, the present paper focuses on the evaluation of HLFC benefits solely on aerodynamic performance. The assessment of the aerodynamic benefit presented in this paper was performed based on numerical simulations of realistic aircraft configurations at cruise flight conditions, including engines with power-on boundary conditions. In particular, the design process and analysis presented in this paper concern the designed wing geometry of the GBD of the HLFC-WIN project. The extended transition prediction capability of the TAU Code for HLFC designs was recently developed in German Aeronautical Research Program LuFo In.Fly.Tec/Aplaus. A further numerical modification introduced in this work, concerns the suction region. State-of-the-art simulation methodologies for HLFC configurations usually consider the effect of boundary layer suction only in the context of transition prediction. In the RANS simulation, however, only laminar and turbulent flow regions are distinguished and the effect of suction on the boundary layer development is not accounted for. In

order to improve the physical representation of surface suction, a direct suction boundary condition was implemented in the TAU solver.

The paper is structured as follows. After the introduction, the aircraft configuration and flow conditions under investigation are presented. A description of the methods used follows. Then results of the shape design are given. The design is described and the analysis of different HLFC/NLF wing designs is presented. Analysis results include a numerical aerodynamic performance assessment for the cruise design point for the HLFC configurations using the *ffd72* far-field drag analysis software of ONERA. After the shape design, the optimization of the suction is presented. Before the summary, results are presented on the improvement of the CFD physical modelling for HLFC configurations. A direct suction distribution is implemented in the DLR TAU code. Results employing this suction boundary condition are presented for an infinite swept wing and a 3D HLFC configuration. Also, a more realistic aerodynamic assessment of the performance of the HLFC design is presented which considers turbulent wedges which occur between the suction panels.

2. Description of the Aircraft Configuration, Flow Conditions & Scope of Geometry Modifications

The studies carried out in this work use the Airbus XRF-1 research large passenger aircraft as a reference geometry [8]-[9]. This geometry contains the fuselage, wing, nacelle, pylon, flap-track fairings and vertical tail plane. A perspective view of the aircraft is shown in Figure 1. CFD computations and far-field analyses consider only half of the aircraft geometry. The geometry corresponds to a target 1g flight shape. The nominal flight conditions at cruise are the following:

$M_\infty=0.83$, $C_L=0.50$, $Re \approx 47 \cdot 10^6$ and a flight altitude of 36,000 ft. Shape design was performed at this point and at off-design conditions with $M_\infty=0.83$,

$C_L=0.50 \pm 0.05$ and $C_L=0.50$ $M_\infty=0.83 \pm 0.02$. For the optimization of the suction distribution, the flight conditions at different flight altitude were considered. These are Flight levels 330, 360 and 390. For each flight level 9 different flow conditions were considered, with $M_\infty=0.81, 0.83, 0.85$ and $C_L=0.45, 0.50, 0.55$. Geometry modifications were restricted to the outer part of the wing, outboard of the leading edge kink and close to the engine position (colour-shaded region in Figure 1), i.e. for span position $\eta \geq 0.319$. A more detailed description of the design requirements is given in section 4.1. The outer wing has 4 suction panels with an individual length of 5 meters. At a first step, a HLFC variant of the XRF-1 aircraft, denoted Airbus 1g HLFC

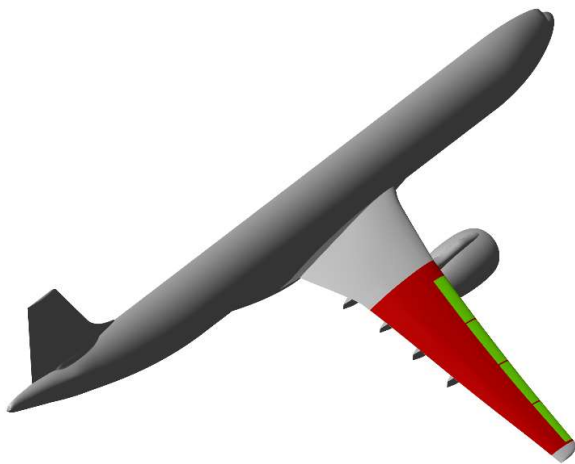


Figure 1 XRF1 geometry indicating outer HLFC wing (red) and leading edge suction panels (green).

geometry was designed by Airbus. Using this geometry as starting point DLR designed a new HLFC wing shape, which is denoted GBD-DLR-2. This design provided the wing surface geometry for the HLFC-WIN ground base demonstrator. A further design is the GBD-DLR-3 geometry, which improves the aerodynamic performance of the GBD-DLR-2 geometry. For a consistent far-field performance analysis among the different configurations, the Airbus 1g HLFC case will not be considered, since it has a smaller spanwise thickness distribution than the reference geometry and the new DLR designs. Further shape designs, which increase the laminar boundary layer extension, are also presented in this work. These are: a) redesign of the inner turbulent wing shape in order to eliminate a λ -shock, which restricts the laminar extent in the outer HLFC wing, b) an NLF design in the region of the outermost suction panel (see Figure 1).

3. Design, Simulation Methods and Postprocessing Tools

The numerical simulations carried out in the course of this work can be classified into HLFC wing shape design, analysis tasks of the shape designs and suction distribution optimization. The following sections describe the methodology, numerical methods and tools used in each case.

3.1 Design method

The DLR inverse transonic 3D design method was used to design the HLFC outer wing [11]. This allows the design of adapted wing sections using user-specified target pressure distributions. The inverse design method is an integrated module of the DLR FLOWer code [12] for block-structured meshes.

The target pressure distributions used are generated with the aim to increase laminar extent and/or reduce shock strength. In the case of HLFC target pressure distributions, also the shape of the pressure distribution in the nose suction region is important. A HLFC pressure distribution presents a suction peak within the suction region. The height and extension of this peak has to be chosen carefully, considering its influence on transition position and shock strength. Furthermore, the change of the suction peak with off-design conditions has to be considered.

The CFD meshes used for the HLFC wing design consider a reduced level of geometrical representation without flap track fairings and engine pylon. They comprise separate wing, body and engine meshes and CFD solutions are obtained using the chimera (overset mesh) technique.

Together with these simplifications, the inverse design method has the advantage that it is a robust, efficient and accurate CFD method, ideal for a large number of design iterations and extensive off-design analysis.

3.2 CFD analysis for complete configurations

For the final analysis of the designed HLFC configurations, the full configuration including flap-track fairings and engine pylon is considered. For this purpose, the wing sections designed with the inverse design process are transferred into a CAD model of the complete aircraft. The CAD model forms the basis for the analysis CFD mesh, which was created using the mesh generator SOLAR [13]. With a resolution of about $30 \cdot 10^6$ mesh points, this mesh is much finer and more complex than the design meshes of about $5 \cdot 10^6$ mesh points.

For the CFD simulations, DLR's flow solver TAU [10] was used. TAU solves the Reynolds-averaged Navier-Stokes equations (RANS) on a cell vertex, finite volume formulation. For the spatial discretization, a central Jameson scheme with matrix dissipation is applied. Time integration is performed with an implicit backward Euler scheme, using LU-SGS. Turbulence modelling was performed with the Spalart-Allmaras SA-negative model.

TAU's iterative automatic transition prediction module [14] is employed to evaluate the local laminar/turbulent transition position for a user-defined number of spanwise stations. At each station, pressure distributions and geometrical data are extracted from the current CFD solution and passed to a differential boundary layer solver. Employing the local conical wing assumption, the solver calculates the local boundary layer profiles. The transition location is predicted by means of local linear stability analysis and a 2-N factor transition criterion, calibrated for HLFC application. The new transition locations for all considered stations form a transition polyline. The transition polyline is then passed back to the CFD solver to distinguish laminar and turbulent parts of the flow. The process of CFD calculation and transition prediction is repeated iteratively. Convergence is usually reached within six iterations. To allow for the treatment of HLFC wing sections, the basic transition prediction module was enhanced to read-in user specified suction distributions. Consideration of the suction distributions in the boundary layer solver then allows for transition prediction for HLFC configurations. In order to improve physical representation of surface suction a direct suction boundary condition was implemented in the TAU solver. Results are presented in section 6. Details on methods and codes involved in the transition prediction module are given in the following section.

3.3 Methods and tools employed for stability analysis and transition prediction

Despite the emergence of more sophisticated stability analysis methods, LST remains the preferred technical tool for stability analysis in computationally intensive design and analysis activities outlined here. Both the design process and the final analysis use the STABTOOL program suite [15]-[16] for transition prediction based on local linear stability theory (LST).

For the stability analysis of 3D wing boundary layers, the assumption of spanwise locally conical flow

conditions is introduced at first. This assumption allows a numerically efficient calculation of the laminar boundary layer profiles per wing section. The boundary layer code *coco* [16] was used to calculate compressible, conical flow boundary layer profiles. *Coco* supports calculations with prescribed boundary layer suction, requiring a special pre-processor provided by G. Schrauf.

To calculate the growth rates of Tollmien-Schlichting (TS) and cross flow (CF) instability modes the local linear stability solver *lilo* [14] was employed. To solve the LST eigenvalue problem, a fixed frequency and fixed propagation direction approach is used for TS waves, while a fixed frequency/fixed wavenumber approach is chosen for CF waves. TS mode evaluation is restricted to a propagation direction of $\Psi=0^\circ$, i.e. along the group velocity direction. For cross flow, only stationary modes ($f=0\text{Hz}$) are considered. Separate N-factors for TS and CF modes are obtained by integrating the respective growth rates along the group velocity direction.

To predict the transition location, a 2-N factor transition criterion is used. The N-factor limit curve was adapted for HLFC design purposes. In addition, the Re_θ criterion is evaluated to check for possible attachment line transition.

3.4 Method for suction panel chambering design and suction distribution optimization

The aim of the aerodynamic HLFC design is to optimize a weighted cost function of laminar drag benefit (e.g. laminar extent) and required suction power. It includes the optimization of a suction distribution, followed by the design of a suitable microperforated suction skin, inner chambering structure as well as inner pressure. The DLR tool chain TASG [7],[17] has been applied, which integrates the boundary layer analysis and transition prediction methods *coco* [16] and *lilo* [15], as well as the suction chamber design program SCDP [19] by Schrauf into a semi-automated HLFC design and optimization process. A basic workflow structure of the TASG tool chain is given in Figure 2. The boundary layer and transition analysis follow the same scheme as described in segment 3.3. The HLFC design and analysis routines also allow for an outer suction skin concept with variable porosity (e.g. pressure loss characteristics) recently developed and wind-tunnel verified in the scope of the LuFo project VarPorHyL / OptiHyL [19]. The results of the aerodynamic HLFC design process, specifically microperforation drilling parameters, chambering as well as inner pressures, suction mass flow and system power estimates are passed on to the system design, manufacturing and overall performance assessment.

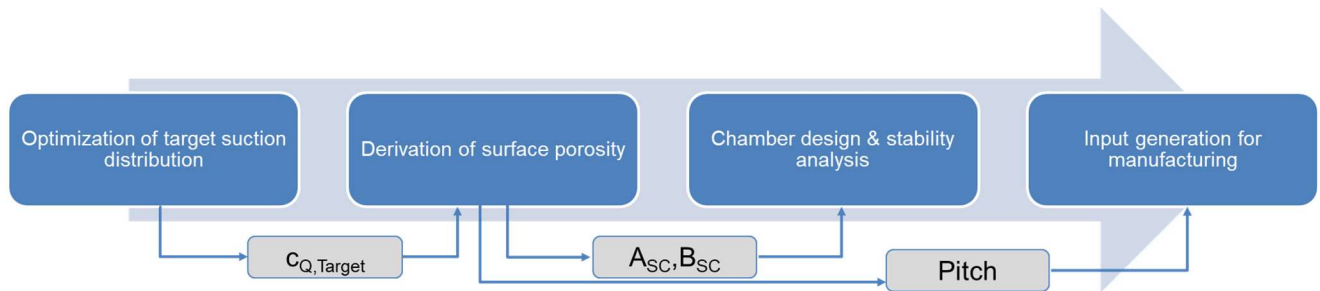


Figure 2: Workflow of the TASG HLFC design process for a suction skin with variable porosity

3.5 Far-field drag analysis method

Standard methods for the computation of aerodynamic forces are based on near-field drag coefficients, which are computed by performing an integration of forces on the aircraft skin. On the other hand, a far-field evaluation of drag components is performed through integrals in the flow field. Such formulations allow a phenomenological breakdown of drag into physical components, namely viscous, wave and induced drag. These provide an essential physical insight into the main sources of drag in the flow field and this into its potential improvement. In addition, a far-field evaluation of drag is more accurate than its near-field counterpart, thus also allowing for a quantification of spurious drag production.

Far-field drag analyses in this work are performed using the *ffd72* post-processing software of ONERA. The formulation and employed methodology are described in [20]-[22]. The far-field method relies on an accurate physics-based definition of control volumes for the integration of viscous pressure, wave and induced drag. The aforementioned software and methodology have been

extensively applied in the research and industry over the past decades.

Near-field drag is defined as the sum of pressure and friction drag:

$$CD_{nf} = CD_p + CD_f$$

Far-field drag on the other hand is defined as the sum of the viscous, wave and induced drag components:

$$CD_{ff} = CD_v + CD_w + CD_i$$

where the viscous drag consists of viscous pressure drag and friction drag:

$$CD_v = CD_{vp} + CD_f$$

Spurious drag production is inherent to numerical computations, and is a product of numerical approximation (e.g. mesh discretization, artificial dissipation). A quantification of spurious drag is made possible through the difference of the two drag calculations:

$$CD_{sp} = CD_{nf} - CD_{ff}$$

Finally, the far-field drag extraction method provides the drag balance:

$$CD_p + CD_f = CD_v + CD_w + CD_i + CD_{sp}$$

Additional variables and performance measures are computed in the case of motorized configurations (see e.g. [20]), in particular specific drag/thrust bookkeeping methods. Results on far-field drag analysis of the HLFC-WIN configurations are also discussed in [23].

4. Shape Design and analysis of HLFC/NLF configurations

In this section, the shape design and analysis of the HLFC and partial NLF surfaces of the outer wing will be described. It includes the shape design of the wing surface for the HLFC ground-based demonstrator. All results shown here correspond to the complete aircraft configuration. They are restricted to the cruise design point.

4.1 Design Requirements

Aerodynamic requirements: The design flow conditions at the cruise design point and off-design conditions correspond to those given in chapter 2. For all flow conditions the active engine boundary conditions (fan intake and primary/secondary stream exhausts) provided by Airbus for the cruise point were used. For the cruise point, the design should not significantly alter the circulation distribution of the Airbus HLFC geometry. This reduces the influence of induced drag changes on overall aerodynamic performance.

Geometry requirements: A detailed HLFC design of the outer wing ($\eta \geq 0.319$) is performed. Thickness requirements are: maintain or increase front spar airfoil thickness and maximum airfoil thickness of the Airbus-HLFC geometry.

Transition position: For HLFC-WIN the laminar region is restricted to the upper side. This is due to the chosen Krueger high-lift system. Current Krueger designs produce surface gaps in retracted position, which make the lower wing surface unsuitable for laminarization. For the shape design, a generic suction distribution was used. It was defined based on the suction distribution used by Airbus for its HLFC design. For consistency with the Airbus results, the transition position was obtained by DLR using incompressible stability analysis and flight incompressible critical N_{TS}/N_{CF} values [24]. However, it is important to mention that for this Mach number: a) a free flight calibration of critical N-factors is not available b) compressible and incompressible stability analysis may lead to designs with different geometry and performance potential [27].

4.2 Shape design methodology and results

In the early stage of the shape design, CFD results were obtained for wing-body meshes and wing-body-engine meshes. A comparison with CFD results obtained for the analysis mesh, which includes all geometry components, showed that: a) for the inverse design it was sufficient and necessary to include the engine in the design process, b) pylon and FTF's could be neglected since their influence was reduced to a local span region.

Although the design was performed on the simplified mesh, all CFD results presented in this subsection, are obtained with the TAU solver for analysis meshes using the complete configuration geometry. Next, the design of the GBD-DLR-2 geometry is described. Figure 3 shows pressure contours for the upper wing for the GBD-DLR-2 design and indicates the region of HLFC wing design. Pressure distributions for the HLFC designs and reference geometry at the wing sections indicated in Figure 3 are given in Figure 4.

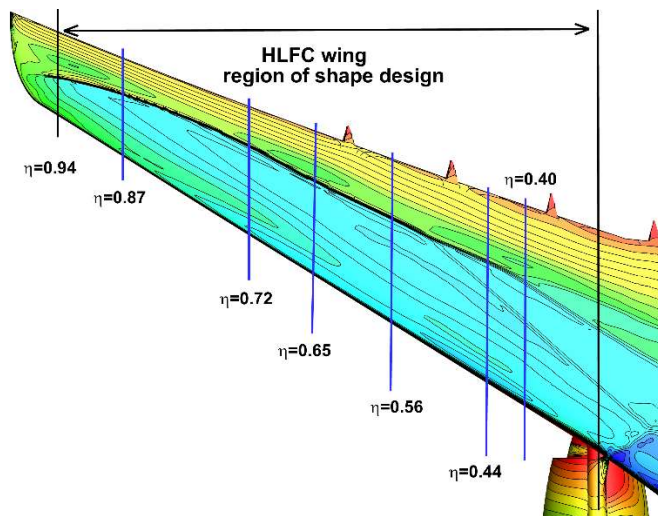


Figure 3 Upper surface pressure distribution contours for the GBD-DLR-2 geometry.

The geometry of the GBD-DLR-2 design was obtained in 2 steps. Since in comparison to the XRF-1 geometry, the Airbus HLFC 1g geometry has a decreased thickness distribution at the outer wing, the first design step was to modify the thickness distribution. For that purpose, the lower side was changed in order to regain thickness. As shown in Figure 4, this leads to a modified GBD-DLR-2 pressure distribution showing a decreased minimum pressure for the lower side. This shape modification was done

without altering the upper wing surface pressure distribution and the local lift value. In comparison to the initial Airbus HLFC design, the maximum airfoil thickness was increased by $\Delta t/c=1\%$ in the outer wing for dimensionless span $\eta > 0.4$. In the second design step, the upper side was considered for the free transition case and target pressure distributions were generated in order to increase the laminar extent of the Airbus HLFC geometry. For that purpose, the target pressure distributions used in the design did not change the shock strength, but changed the nose suction peak and the pressure gradient. Figure 4 shows the pressure distribution of the finally designed GBD-DLR-2 geometry using these target pressure distributions. They are compared to the pressure distributions of the Airbus HLFC 1g geometry and the XRF-1 reference geometry. The leading edge region of the HLFC design airfoils generally exhibits lower leading edge radii and reduced curvature. As a result, this leads to a reduced pressure gradient in this region on the pressure side. Overall, both HLFC geometries exhibit a more regular acceleration of the flow up to roughly 30%-40% of the chord on the pressure side than the reference wing, a favourable effect for the preservation of a laminar flow. On the suction side and at the outboard part of the HLFC wings pressure distributions are quite different from that on the reference configuration. The acceleration following the most forward weak recompression (which is overall weaker for the HLFC wings) is favourable for the delay of transition. In addition, the upstream recompression can limit the intensity of shockwaves despite the acceleration over an important portion of the chord. The reference turbulent wing overall shows an arrangement of multiple shock waves. HLFC wings on the other hand aim at extending the laminar region by presenting a more progressive acceleration, which leads to a single shock wave around 60% of the chord. Multiple shock waves occur for the fixed geometry inner wing but also closer to the wing tip, at $\eta=0.87$, where the reference geometry results in a first shock closer to the mid-chord position, followed by a decompression and a second shock further downstream. HLFC geometries however result in a more progressive acceleration up to a single shock formed in an intermediate position with respect to the two shocks of the turbulent wing. Concerning the pressure coefficient evolutions of shockwave location, the comparison between fully turbulent and laminar/turbulent computations on the HLFC wings shows an important difference. Differences on the pressure coefficient are already observed at $\eta=0.40$. The shockwave position is moved further downstream in the laminar/turbulent cases, compared to the fully turbulent computation of each corresponding HLFC configuration. The transition position and shock position are given in Figure 5. The GBD-DLR-2 design is also influenced by the flow properties of the fixed shape inner wing. The inner wing shows a complex shock system. Unfortunately, the

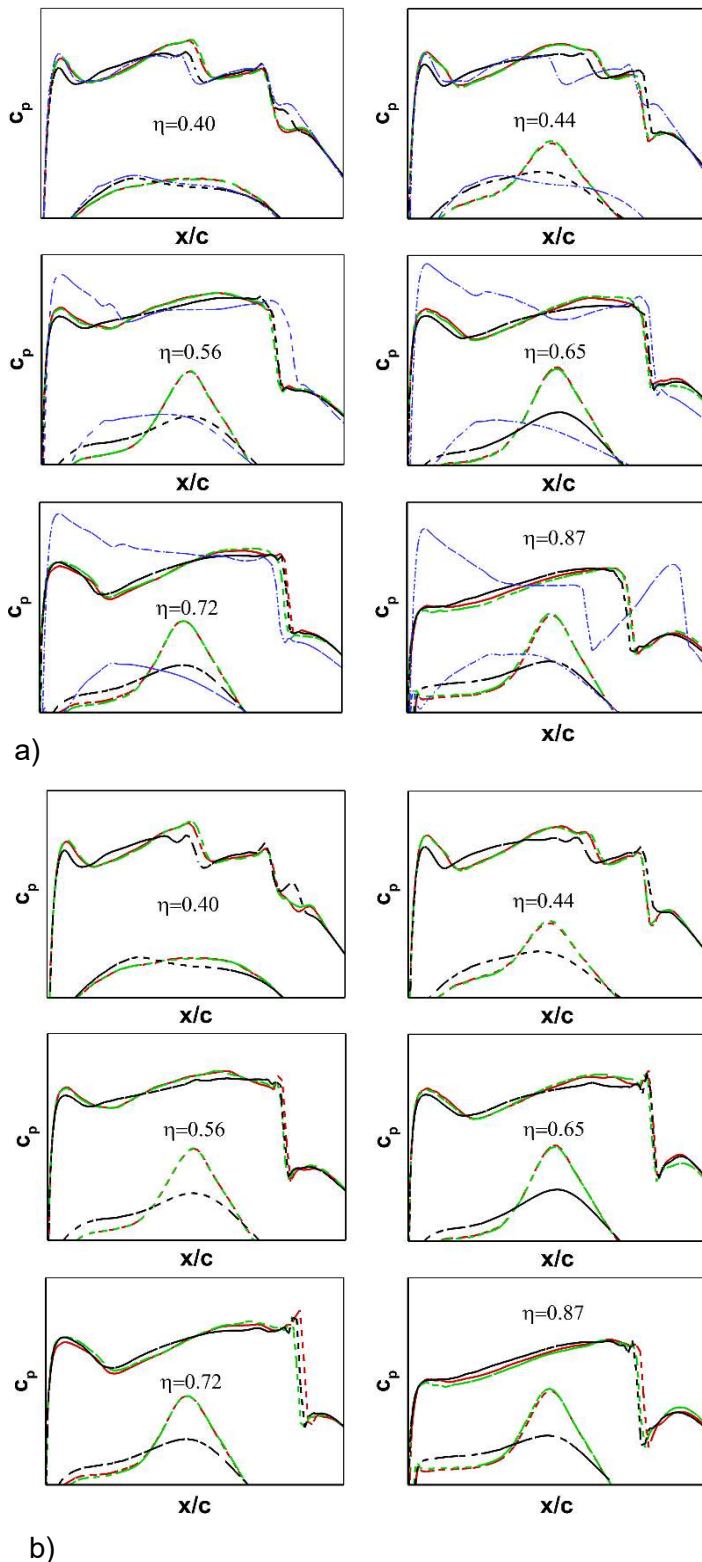


Figure 4 Pressure distribution for outer wing sections. Results for the Airbus HLFC 1g (black), GBD-DLR-2 (green), GBD-DLR-3 (red) and reference XRF-1 geometry (blue). Upper side a) is for turbulent boundary layer and lower side b) is for the free transition case.

to the latter case in induced drag and pressure distribution for inner wing and body should be reduced. In comparison to the GBD-DLR-2 geometry, the GBD-DLR-3 shows an improved overall aerodynamic performance (see section 4.3) and a slightly increased laminar boundary layer extent (see Figure 5). Results show that the circulation distributions for the designed geometries are very similar to the circulation distribution of the Airbus HLFC 1g configuration (results not shown here).

leading edge part of the λ -shock (see Figure 5) that originates from the inner turbulent wing (wing root section) partially restricts the extension of laminar boundary layer in the outer wing part (HLFC wing part). This is seen in the pressure distribution for sections $\eta=0.40$ and $\eta=0.44$ (see Figure 4), where the more upwind placed shock will lead to a transition. In Addition to the λ -shock, Figure 5 shows an inner wing shock originating at the inboard pylon wing intersection. These shocks merge with the most downwind placed shock, which in turn limits the supersonic upper wing region.

The GBD-DLR-2 geometry has a larger laminar extent with respect to the Airbus HLFC 1g geometry case by an additional 1.7% of the wing surface. However, as will be shown in the far-field drag analysis in section 4.3 the GBD-DLR-2 configuration showed an increase of wave drag in comparison to the reference and the Airbus HLFC 1g geometries. This wave drag increase occurred around a region of span position $\eta=0.6$. This occurs despite the GBD-DLR-2 and the Airbus HLFC configuration showing no significant difference in shock strength in the pressure distributions. Therefore, an additional geometry was designed denoted GBD-DLR-3. Target pressure distributions used for the GBD-DLR-3 case feature a slightly larger recompression between the transition position and the shock. As shown in Figure 6 for the pressure distribution of wing section $\eta=0.65$, the finally designed GBD-DLR-3 shows this property. Furthermore, the GBD-DLR-3 geometry was designed in such a way that the angle of attack for which the cruise design point lift value is achieved is closer to the angle of attack at which this occurs for the Airbus HLFC 1g geometry. Thus, differences

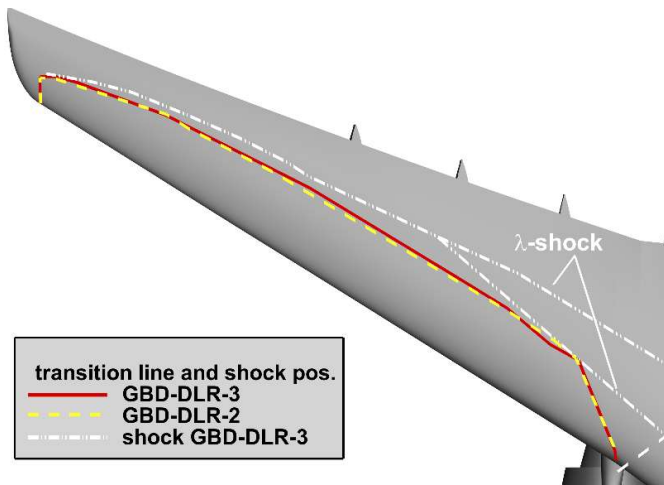


Figure 5 Free transition position for HLFC outer wing and shock position.

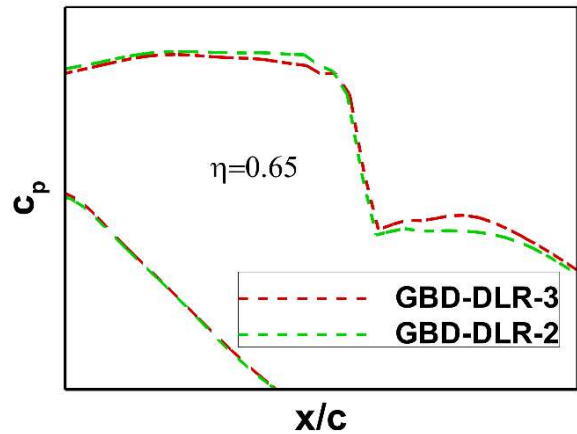


Figure 6 Comparison of pressure distribution in the shock region for $\eta=0.65$. Solutions for turbulent boundary layer with analysis mesh.

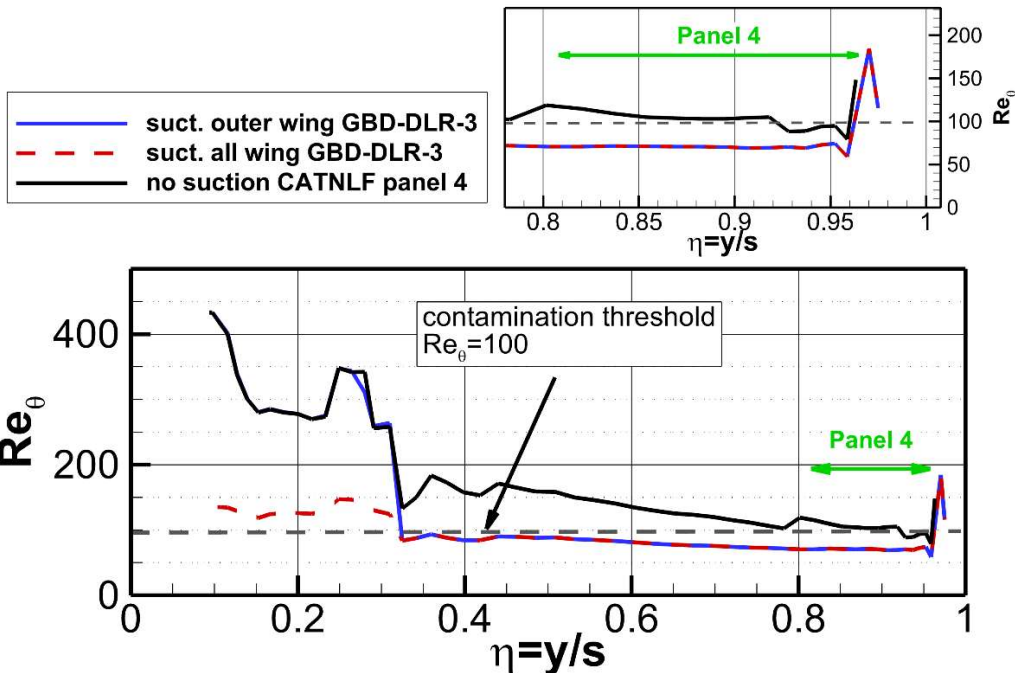


Figure 7 Attachment line criterion Re_θ

Besides transition due to crossflow and Tollmien-Schlichting instability, transition due to attachment line instability should also be considered. For suction cases the attachment line criterion used here is Re_θ based on θ^* [25]. For cases without suction the attachment criterion used is \overline{Re} [26]. For these cases Re_θ is computed using $Re_\theta = 0.4044 \cdot \overline{Re}$. Figure 7 shows the attachment line criterion Re_θ as a function of the dimensionless span position for the GBD-DLR-3 wing geometry. Note that no attachment line transition is expected for the outer HLFC wing ($\eta > 0.310$), since Re_θ values are less than 100, the contamination threshold. Besides the contamination threshold itself, the transition threshold with a value of $Re_\theta = 235$ should also be considered, beyond which there will be attachment line transition.

All results presented so far in this section are for the cruise design point. In the design process, off-design conditions were also considered but these results will be presented in the section 5 alongside results on the optimization of the suction distribution.

4.3 Cruise aerodynamic performance of designed HLFC configurations

Laminar/turbulent computations, often consider suction only in transition prediction. This naturally only influences the laminar region extent, as the boundary conditions employed do not include active suction across the surface, but still has a significant impact on skin friction. Figure 8 shows a skin friction distribution at a 60% wingspan position for the five different cases. The reduction of skin friction for the laminar region of the flow is clearly visible and at this spanwise position is shown to extend across an important part of the chord. As expected, this reduction of skin friction is not observed in the case of fully turbulent flow over the same geometries. Furthermore, between the two HLFC wings, the GBD-DLR-3 shows a slightly lower skin friction at the end of the laminar region.

Global lift and near-field/far-field drag coefficient increments of the HLFC configurations are presented in Table 1. The reference values for these increments are those of each corresponding coefficient of the reference XRF-1 aircraft. Note also, that the computed solutions correspond to approximately the same lift coefficient, which results in a different angle of attack of each configuration. A first comparison can be performed in fully turbulent conditions between the two HLFC geometries and the reference XRF-1.

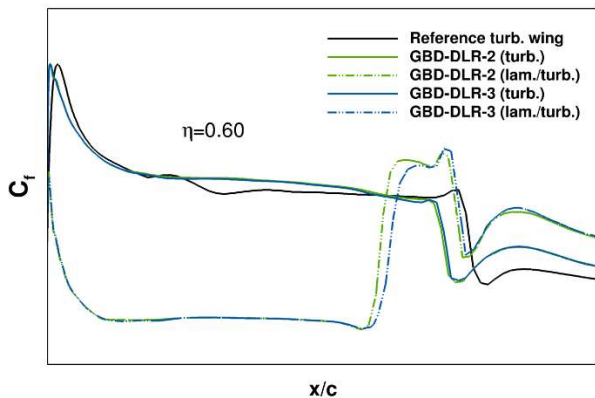


Figure 8 Friction coefficient across the upper wing surface at $\eta=0.60$ for the reference aircraft and its HLFC variants in fully turbulent and laminar / turbulent (free transition) conditions

In practice a number of flight events and conditions may lead to such a wing being operated in a regime of reduced laminar region extent. Despite the fact that fully turbulent conditions correspond to the worst-case scenario in that aspect, this comparison already provides an interesting evaluation of nominal performance degradation. Friction drag is similar for the three fully turbulent computations, with differences of HLFC geometries compared to the reference being lower than 0.5%. The total near-field drag difference is thus mainly attributed to the pressure drag component, the differences on which are notably between the two HLFC geometries at fully turbulent conditions and the reference turbulent one. A far-field drag decomposition of the total drag

force highlights that the main contribution to this is a notable increase of wave drag. This pressure drag penalty in turbulent conditions is reduced on the GBD-DLR-3, because of geometry modifications aiming at reducing the wave drag identified in the far-field drag analysis of the GBD-DLR-2 geometry (see section 4.2). The tabulated relative values on this drag component are high due to absolute wave drag levels being low on such a reference transonic wing. In addition, it is important to note that, the geometry modifications applied in the HLFC wings result in a viscous pressure drag reduction with respect to the reference XRF1 aircraft, even in turbulent flow. Despite this benefit however, HLFC wings result in an increased overall far-field drag value compared to that of the reference aircraft.

In contrast, the consideration of boundary layer laminarization in free transition laminar/turbulent computations shows that both HLFC geometries exhibit a reduced overall far-field drag compared to the reference configuration. Near-field drag values show that this benefit is obtained in both the pressure and friction drag components. A more detailed insight is then obtained by a phenomenological far-field drag breakdown. This highlights a significant reduction of the viscous pressure drag component, which in terms of absolute increment value is of the same order of magnitude as that of friction drag. This viscous pressure drag benefit is also more important in the case of the GBD-DLR-3 configuration than for the GBD-DLR-2. In terms of wave drag penalty of the HLFC geometries, results show that this is still observed in laminar/turbulent computations, but is

lower compared to the case of fully turbulent flow around the same geometries. Finally, both HLFC geometries also show a reduction in terms of induced drag, which is more significant in the case of the GBD-DLR-3. The overall improved aerodynamic performance of this latter configuration compared to the GBD-DLR-2 is thus apparent, in particular in terms of overall far-field drag. It is also important to note that the modifications introduced for the reduction of the wave drag penalty do not degrade aerodynamic performance in terms of any individual drag component with respect to the GBD-DLR-2.

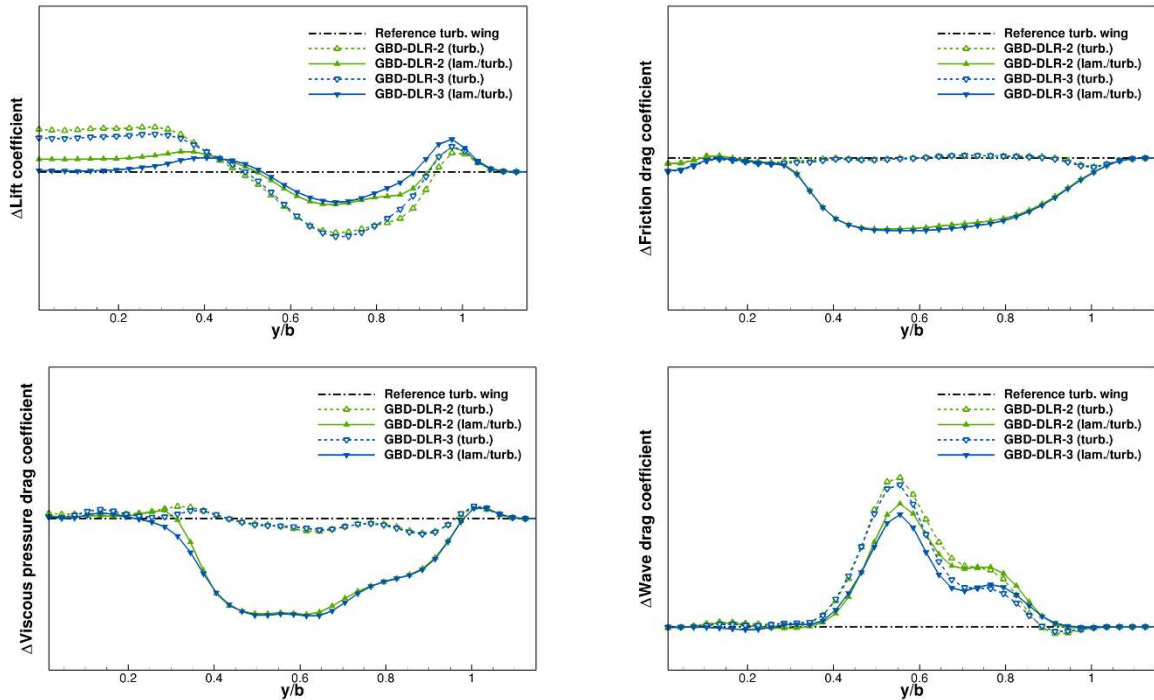


Figure 9 Approximate spanwise distribution of near-field and far-field coefficient increments with respect to the reference XRF-1 aircraft, computed with the ffd72 software.

The above results highlight the importance of an accurate far-field drag assessment. First, an accurate far-field drag analysis can provide a considerably increased precision compared to a near-field evaluation of drag, and thus a more accurate quantification of the drag benefit due to laminarization. On the other hand, the breakdown of drag into physical components, is essential to the improvement of the aerodynamic design and the accurate understanding of the physical mechanisms involved therein. When only having access to near-field drag components, it is likely to interpret the friction drag reduction as being the principal mechanism involved in the laminarization benefit. As expected however, the far-field breakdown shows that the benefit of laminarization is in fact distributed between the viscous pressure drag and friction drag, and thus prevents the viscous pressure drag benefit from being masked by a wave drag or induced drag contribution. Hence, a far-field drag analysis thus indicates the possibility of separately addressing the issue of the wave drag penalty in such a case. The importance of this insight is demonstrated by the improved performance of the GBD-DLR-3 geometry, compared to the GBD-DLR-2. An improvement is observed both in terms of a larger drag benefit due to laminarization and in a reduction of the drag penalty if the wing is operated in fully turbulent conditions.

Finally, Figure 9 presents approximate spanwise distributions of aerodynamic coefficient increments for the different computations. These are an important complement to global drag component values, as they can guide aerodynamic design by the identification of areas responsible for performance degradation, or areas of potential for performance improvement. The distributions are consistent with the global drag coefficient increments presented in Table 1. In terms of lift, the distributions indicate that HLFC configurations present a slight transfer of loads towards the inboard part of the wing, which

is more notable on fully turbulent computations compared to laminar/turbulent ones. Both the friction and the viscous pressure drag distributions clearly depict the effect of laminarization on the outboard part of the wing, alongside with minor modifications near the engine position. The wave drag increase on the outboard part of the wing is also clearly identified, with an overall similar trend between the two HLFC configurations.

Geometry	Transition type	AoA (°)	ΔC_{Dp}	ΔC_{Df}	ΔC_{Dvp}	ΔC_{Dw}	ΔC_{Di}	ΔC_{Dsp}	ΔC_{Dff}	Laminar surface [%]
XRF-1	Turbulent	2.634	-	-	-	-	-	-	-	-
GBD-DLR-2	Turbulent	2.781	+2.05%	-0.15%	-1.79%	+99.77%	+0.85%	-20.90%	+2.27%	-
	Free Transition	2.682	-1.13%	-4.69%	-16.92%	+85.29%	-0.20%	-10.17%	-2.86%	14.26 %
GBD-DLR-3	Turbulent	2.745	+1.55%	-0.35%	-1.64%	+83.91%	+0.33%	-17.51%	+1.59%	-
	Free transition	2.637	-1.85%	-5.01%	-19.19%	+70.11%	-0.52%	-19.21%	-3.71%	14.42 %

Table 1 Near-field and far-field drag coefficient increments (w.r.t. the reference XRF-1 aircraft) computed with the fd72 software for the two HLFC geometries in fully turbulent and laminar/turbulent conditions at cruise. The laminar surface percentage is computed with respect to the wing surface, excluding the pylon and FTFs.

4.4 Further shape designs

In this section further shape design work is presented. Additional designs were performed with the aim to show further potential of laminar flow for the considered geometries. These studies were performed using the simplified design mesh, i.e. the geometry consisting of wing-body-engine. Initial geometry for this study is the GBD-DLR-3 geometry.

4.4.1 NLF design in tip region

A further design considered in this work is an NLF design in the region of the fourth suction panel with position close to the tip (see suction panels in Figure 1). A NLF design is possible in this region if transition due to crossflow is avoided in the nose region by using CATNLF design [27],[28],[29]. The intended NLF region had a span extension of $0.82 < \eta < 0.96$. To allow a smooth transition from the HLFC region to the NLF region, the wing was also modified in the span region of $0.76 < \eta < 0.82$. Figure 10 shows the redesigned CATNLF pressure distribution for $\eta = 0.87$ in the nose region. In order to avoid a transition due to crossflow without using suction the redesigned pressure distribution has a much steeper acceleration in the nose region. The minimum value is achieved already for $x/c = 0.003$. After this point, a region of constant pressure distribution follows. Typically, the larger the pressure gradient is, the larger will be the growth of crossflow N-factor. However, very close to the nose the growth of the crossflow N-factor still is small. Therefore, the redesigned pressure distribution shown in Figure 10 attenuates the growth of crossflow modes in the nose region by placing the required pressure gradient as close to the nose as possible. In order to have a large NLF extent, the pressure distribution should also to be modified in the region between the nose and the shock. The redesigned pressure distributions for this region are shown for several sections in Figure 11. Note that the pressure distribution has been changed in such a way that the shock of the CATNLF designs occurs further downstream of the GBD-DLR-3 design, also for the sections closer to the wing tip. The transition position and shock position of the CATNLF design are compared to the GBD-DLR-3 design in Figure 12. Incompressible critical NLF and HLFC N-factors are used to obtain the transition position. Figure 12 also shows the NLF transition position for the GBD-DLR-3 geometry for the case where no suction is applied in the outermost panel. The transition occurs due to crossflow instability and is close to the leading edge. In this case and for the CATNLF design the transition position is obtained using the incompressible HLFC critical N-factors for the region $\eta < 0.82$, whereas for the region $\eta > 0.82$ the incompressible NLF critical N-factors are used. For the span position where the 4th panel begins, the CATNLF design shows a transition close to the leading edge. However, it is not possible to obtain a laminar boundary layer at this point since a turbulent wedge will occur at this

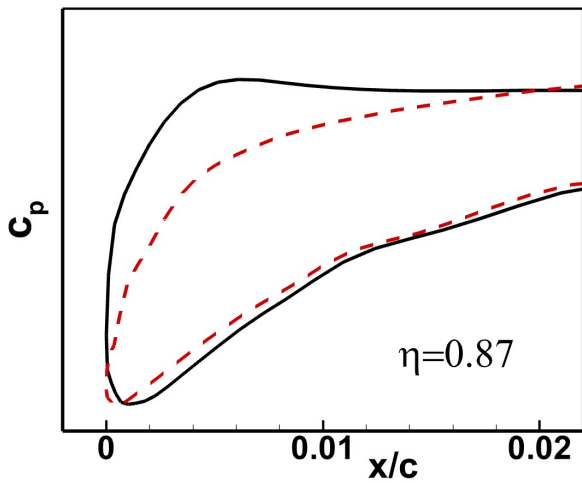


Figure 10 Pressure distribution for $\eta=0.87$ in nose region for GBD-DLR-3 design (red dashed line) and HLFC & NLF design (black).

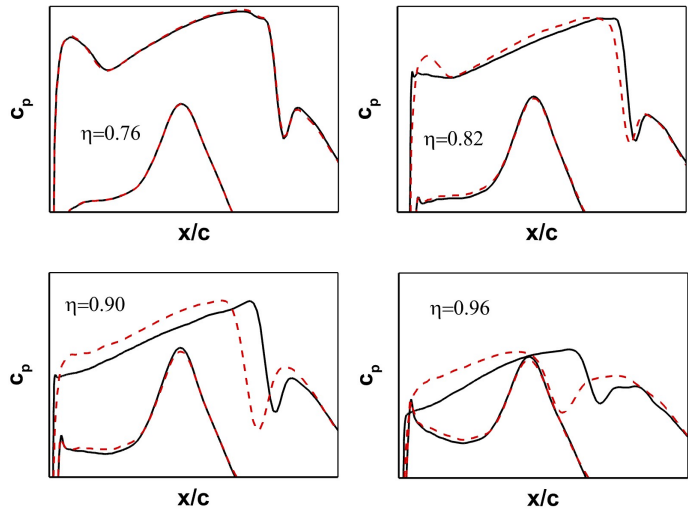


Figure 11 Pressure distributions for various sections for GBD-DLR-3 design (red dashed line) and HLFC & NLF design (black).

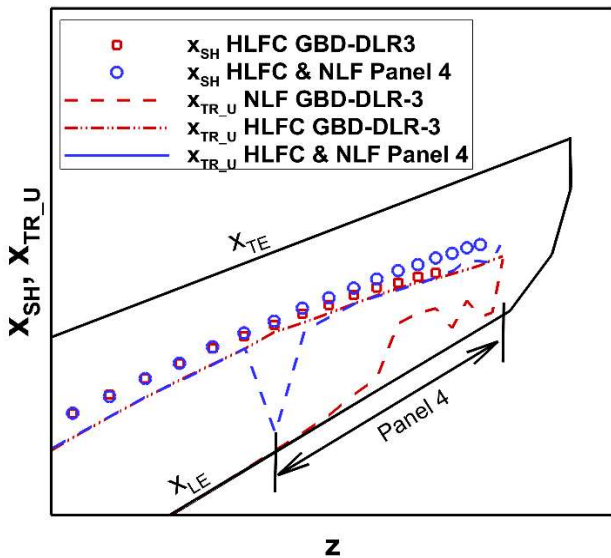


Figure 12 Transition and shock position for GBD-DLR-3 design (red dashed line) and HLFC & NLF design (black)

span position. For larger span positions the transition point of the CATNLF design is similar to the one obtained with suction for the GBD-DLR-3 geometry. The results for the attachment line criteria for the CATNLF design are also given in Figure 7. Note, that Re_0 values increase for the CATNLF without suction, in comparison to the GBD-DLR-3 geometry. In panel 4 these values are slightly larger than the contamination threshold $Re_0=100$. The shape design study performed in this section shows that an NLF design is possible for the region of panel 4. Using the incompressible critical N-factors it is difficult to obtain an NLF design for span positions smaller than the one of panel 4. However, a CATNLF design could be used for the inner suction panels to reduce the required suction.

4.4.2 Inner wing design to eliminate the λ -shock

As mentioned before, the leading edge part of the λ -shock (see Figure 5) that originates from the inner turbulent wing (wing root section) partially restricts the extension of laminar boundary layer in the outer wing part (HLFC wing part). Therefore, using inverse design with target pressure distributions in which the leading edge part of the λ -shock is eliminated, a shape design was performed in the inner wing. A geometry was obtained which leads to pressure distributions where the leading edge part of the λ -shock was eliminated. With the modified inner wing geometry, a new redesign of the outer HLFC wing

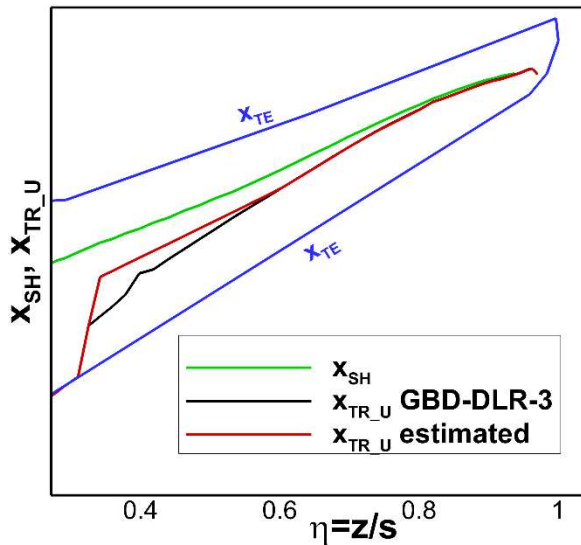


Figure 13 GBD-DLR-3 shock position (green) and transition line (black) and estimated transition line after removing upwind λ -shock (red).

was not performed. Instead it was possible to compute an estimate in terms of additional drag reduction due to the added extent of the laminar boundary layer, under the assumption that a new transition line placed further downstream can be obtained in the outer HLFC wing after eliminating the upwind λ -shock. In Figure 13, a comparison is shown between the GBD-DLR-3 upper wing transition line (results from the design mesh) and the new estimated line. The modified transition position is assumed at 50%c. In the case of the section for $\eta=0.40$, shown in Figure 4, this means changing the pressure distribution so that transition occurs at a position which is 10%c further downstream. Note that the new transition position has a safety margin to the shock position. Target pressure distributions are assumed, which have a positive pressure gradient between estimated transition position and shock. This is assumed in order to allow a smaller shock strength. Therefore, it is assumed that the original GBD-DLR3 shocks can be retained in the

modified region, i.e. a geometry can be achieved with the estimated transition position without a wave drag increase. Using the pressure distributions from the GBD-DLR-3 geometry but assuming that the transition position moves to the estimated transition, preliminary estimates indicate that the relative drag reduction for the free transition case of the GBD-DLR-3 configuration would change from 3.71% to a value 4.12%.

5. Optimization of suction distribution and chambering design

In this section, the HLFC design for the GBD-DLR-2 configuration for various cruise conditions is described. The design is based on surface pressure distributions at the medium spanwise location of all 4 HLFC segments, as sketched in Figure 14. Additional sections at the segment boundaries are used to check, whether the spanwise variation of surface pressure has an effect on the HLFC design. The change of flight conditions was found to have a significant influence on the pressure distribution. Especially the suction peak, which spans the region of surface suction upstream of the front spar, is changed significantly in height and widths. To highlight the challenges, those variations have with respect to the HLFC design, Figure 15 gives

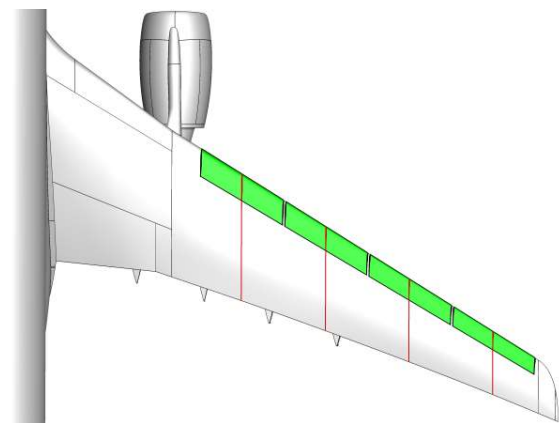


Figure 14 Pressure section cuts for HLFC design

an overview of the influence the parameters lift coefficient, Mach number and flight level have on the pressure distribution at a mid-section of segment 3. The lift coefficient and Mach number are clearly dominant here, while a flight level variation has only minor influence. The minimum pressure on the suction peak dictates the duct pressure level and with that the system requirements, such as compression and mass-flow rate. At the same time, an increased pressure gradient induces a higher cross-flow amplification rate, which needs to be damped by higher local suction rates. The chordwise

extent of the suction peak becomes an issue, when the area of pressure recovery exceeds the suction area. Without the presence of surface suction, a positive pressure gradient leads to high Tollmien-Schlichting amplification rates, potentially causing early transition. A critical case can be seen in the left image for the maximum lift coefficient. A secondary Mach number influence is the chordwise shift

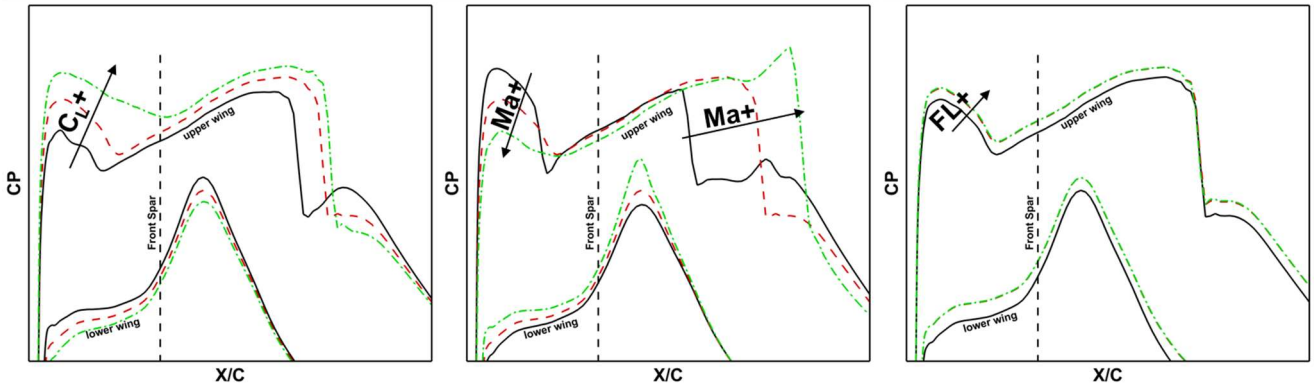


Figure 15 Surface pressure distributions at spanwise location $\eta = 74\%$. Variation of lift coefficient (left), Mach number (middle) and flight level (right).

of the shock. For low Mach numbers, this may be a limiting factor for the laminar extension, which cannot be directly be influenced by the suction system design. The critical design cases for the HLFC system are therefore the minimum Mach number and high lift coefficient cases. Low flight levels are also more critical due to the higher Reynolds numbers and higher mass-flow requirements due to the increased air density. The critical design point within the HLFC envelope is $FL = 330$, $Ma_{\infty} = 0.81$ and $C_L = 0.55$.

As a first design step, a target suction distribution was optimized for each segment, maximizing the laminar extent, while penalizing high integral suction rates. Figure 16 illustrates the following porosity design process, starting from the target suction distribution, a red dashed line. The next step is to

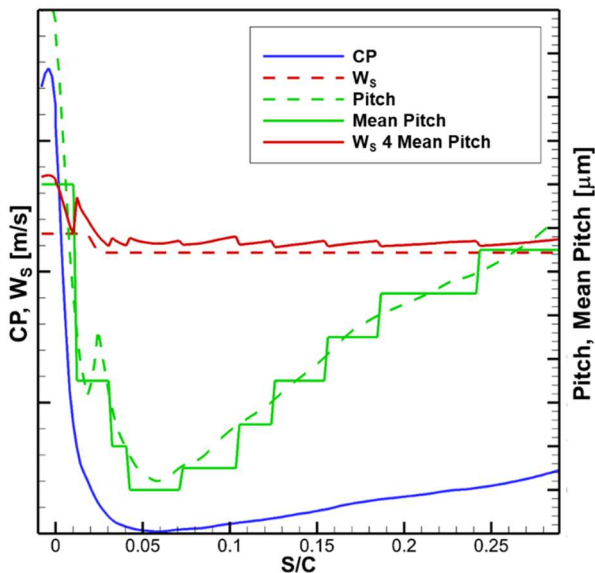


Figure 16 Exemplary pressure, suction and pitch distribution.

derive a suitable porosity distribution of the microperforated outer skin at a given duct pressure. The surface porosity can be altered by changing the hole diameter or the pitch. Since the hole diameter is closely coupled to elaborately adjusted settings of the applied laser drilling process, the pitch is usually solely used to adjust the surface porosity. Using a relation between surface porosity and pressure loss, established by Preist and Paluch in [30], the pitch distribution can be directly derived. In order to make this continuous distribution feasible in terms of manufacturing, it is discretized in steps of $50\mu\text{m}$ (green solid line). Furthermore, certain limits for the pitch have to be respected: In order to avoid adverse interaction of vortices, emanating from suction holes, the pitch needs to be larger than 10 times the hole diameter [31]. The upper pitch limit was chosen to $1400\mu\text{m}$, an order of magnitude below the expected blockage due to structural

stiffeners, in order to avoid premature transition, should several subsequent holes in local flow direction be blocked. Furthermore, choking and additional aerodynamic roughness due to the over-

suction phenomenon, introduced by Pfenninger [32], had to be avoided. The resulting suction distribution, is drawn as a red solid line. A higher suction area around the leading edge is due to upper pitch limit, but will also help avoiding attachment line transition (ALT).

The chamber and porosity design were performed for each HLFC segment and all points of the HLFC flight envelope. The resulting system requirements for one complete wing ranged between 440 and 700 g/s of suction mass-flow and 35 to 44 kW of suction power. This large spread in system requirements throughout the envelope is due to the above-mentioned variation in surface pressure. The given power offtake factors into the estimation of overall block-fuel reduction as a penalty term.

6. Improvements of CFD Analysis for HLFC cases

The numerical work on HLFC configuration development at DLR has so far focused on the aspect of laminar/turbulent transition prediction. In this context, transition analyses for HLFC configurations have been performed using script-based methods described in Section 3.3. Determined transition positions must be manually prescribed to the flow solver.

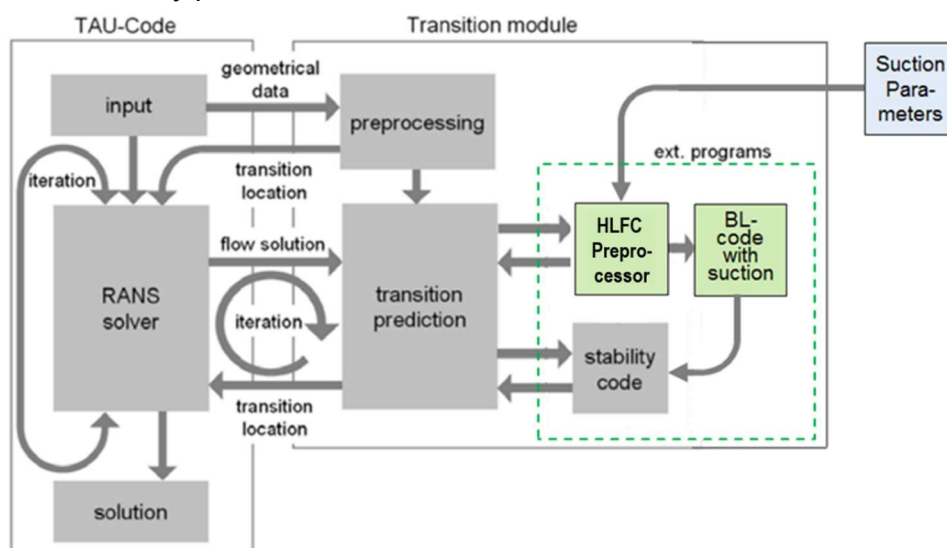


Figure 17 Process flowchart of the TAU code with coupled transition prediction with HLFC extension

To facilitate the work in the future, the transition module of the TAU code was extended for LST-based transition predictions with boundary layer suction. Figure 17 shows the workflow of the TAU RANS solver with coupled transition prediction, enhanced for HLFC applications. The main change to the current transition prediction scheme for NLF applications [33] is the addition of an HLFC preprocessor for the boundary layer procedure involved. Via this preprocessor, the local boundary layer suction can be specified either in the form of a suction coefficient distribution or via porosity parameters and chamber pressure of the suction system.

The new process allows for fully automatic transition prediction in RANS simulations at an arbitrary number of wing sections. Simultaneous treatment of NLF and HLFC areas of a configuration is possible.

An important issue for accurate flight performance predictions of HLFC simulations is the consideration of boundary layer suction in the RANS solver. Although the pressure distribution is hardly changed by weak boundary layer suction the influence on the boundary layer profiles is significant. They become more full-bodied and the boundary layer thickness is reduced. On the one hand this leads to the desired stabilization of the laminar boundary layer, on the other hand the wall shear stress increases and the momentum loss thickness decreases in comparison to a laminar boundary layer without suction. In three-dimensional boundary layers the crossflow component is reduced by suction due to the increase of streamwise momentum.

Until now, the effects of boundary layer suction on boundary layer development and flight

performance could not be considered with the TAU code, since corresponding suction boundary conditions were missing. Only laminar and turbulent regions could be distinguished via the boundary condition, and suction was neglected. To overcome this apparent gap in physical modelling, two different boundary conditions for boundary layer suction were implemented:

- Suction coefficient boundary condition (BC1)

A suction coefficient CQ is explicitly assigned to each surface grid node of an area defined by a surface marker. The local wall normal suction velocity w_s is calculated as follows:

$$w_s = CQ \cdot U_{inf}$$

- Porosity Parameter and chamber pressure boundary condition (BC2)

The wall normal suction velocity of each grid node of an area defined by a surface marker is calculated from given surface porosity parameters A_{sc} and B_{sc} , the chamber pressure p_c of the suction system and local flow variables of the RANS solver at the surface node.

Rearranging the empirical pressure loss relation of Preist and Paluch [30], a quadratic equation for the mean local suction velocity is obtained:

$$w_s = -\frac{A}{2B} + \sqrt{\left(\frac{A}{2B}\right)^2 + \frac{p_s - p_c}{B}}$$

with

$$A = A_{sc} \frac{\mu_s}{\mu_0}, \quad B = B_{sc} \frac{\rho_s}{\rho_0}, \quad p = \text{pressure}, \quad \mu = \text{viscosity}, \quad \rho = \text{density}$$

Here, A_{sc} and B_{sc} are parameters that depend on various properties of the porous suction surface (see [28] for details). Values for A_{sc} and B_{sc} must be determined experimentally. The viscosity and density ratios $\frac{\mu_s}{\mu_0}$, $\frac{\rho_s}{\rho_0}$ account for the influence of flight altitude on suction. The index s denotes properties at actual flight conditions at the surface, while index 0 denotes conditions under which A_{sc} and B_{sc} were determined.

For each of the suction boundary conditions values, (either CQ or A_{sc} , B_{sc} , p_c) have to be assigned to the point IDs of the CFD surface mesh. In the simplest case of constant values per surface marker, the values can be directly specified in the parameter file of the TAU code. In order to specify spatially varying suction distributions or variable porosity/chamber pressure distributions, it is required to create an input file, containing the required information for the boundary condition.

Commonly, suction distributions or porosity and chamber pressure distributions are defined in terms of the non-dimensional natural profile coordinate s/c . To facilitate the mapping of data defined in terms of s/c to the point IDs of a 3D wing surface grid, a dedicated algorithm has been developed that creates the required input file for the suction boundary condition.

The mapping algorithm detects the edges of the suction marker from the CFD grid (cartesian coordinates) and creates a bi-parametric surface representation in terms of s/c and a spanwise

The explicit suction boundary condition (BC1) is particularly useful when a certain suction distribution is given. This is the case e.g. for single point analysis and for validation against analytic or experimental data. For performance evaluation of HLFC systems over the entire flight envelope, the use of BC2 is clearly preferable. Instead of imposing a new CQ distribution for every flight condition, the suction boundary condition has to be set-up only once and remains valid for all flight conditions. Required adjustments of the chamber pressure can be controlled via parameter file. The shortcoming of BC2 is, that it is not applicable to HLFC systems where chamber pressures are dependent on duct pressure (e.g. ALTTA HLFC concept, see [34]).

6.1 RANS solutions with suction boundary condition

After successful validation of the suction boundary conditions against experimental data [35],

simulations were carried out on an infinite swept wing model. The model with a sweep angle of $32,5^\circ$ was designed to represent the design pressure distribution at the outer wing of the GBD-DLR-2 configuration. The simulations were performed at the following conditions: $Ma=0.83$, $c_L= 0.546$, altitude =36000ft. A generic CQ distribution (Figure 18) was specified for the suction boundary condition (BC1) of the RANS solver. To assess the effect of boundary layer suction on the results, the simulation was repeated without suction. As shown in Figure 19, the effect of suction on the pressure distribution is very small, as expected. The only noticeable deviation is found upstream of the shock position on the upper surface. Significant, however, is the increase in the wall shear stress coefficient c_{fx} as a result of suction. Compared to the laminar boundary layer without suction, skin friction is twice as high with active boundary layer suction. Downstream of the suction region, the values of c_{fx} rapidly equalize to the case without suction. The development of streamwise integral boundary layer data is shown in the right part of Figure 19.

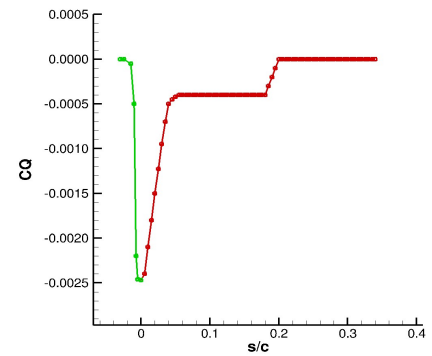


Figure 18 Generic CQ-distribution. Green: lower surface, red upper surface

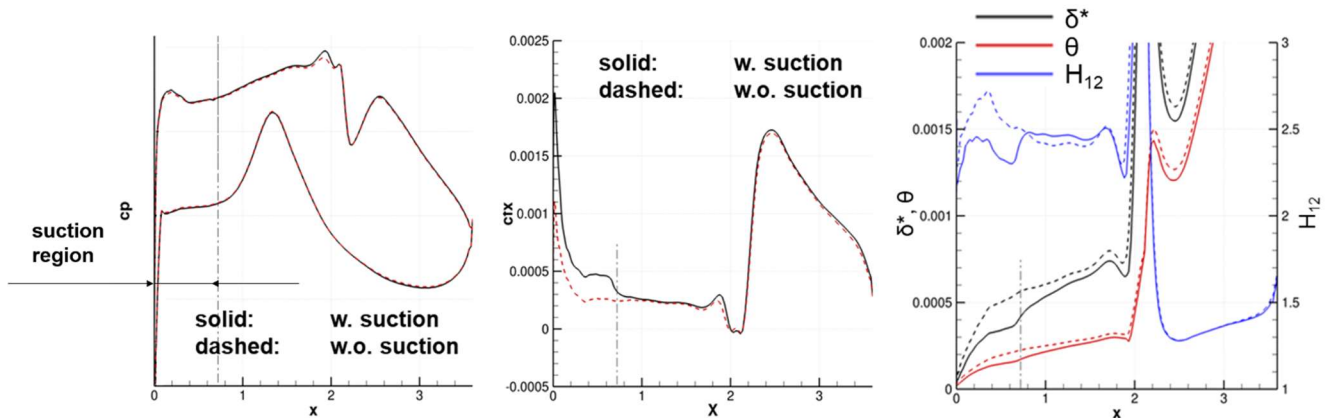


Figure 19 Comparison of results with and without boundary layer suction for the infinite swept wing model. Left: c_p -distribution, center: skin friction coefficient c_{fx} , right: integral boundary layer data.

Suction reduces both, displacement thickness δ^* and momentum loss thickness θ to different extents. As seen from the shape factor $H_{12} = \delta^*/\theta$, the relative reduction of δ^* is larger than that on θ . Compared to the case without suction, the shape factor H_{12} is smaller in the case with active suction. It is noteworthy that the reduction in boundary layer thicknesses due to suction persists well beyond the suction region. Even in the turbulent region downstream of the shock, it remains discernable. The thinner boundary layer and the more full-bodied velocity profiles are responsible for the observed increase in skin friction.

Evaluating the simulation results for the infinite swept wing testcase with respect to drag, an increase of 3.2% is observed when boundary layer suction is accounted for in the RANS simulation. Drag due to friction increases by 7.4% while the pressure drag is reduced by 1.2% compared to the case without suction.

Application of the suction boundary conditions to the GBD-DLR-2 Testcase

With regard to the significant change in resistance due to active boundary layer suction for the infinite swept wing test case, it is now of interest how strong the influence is on a full configuration. For this purpose, systematic investigations were performed on the GBD-DLR-2 configuration in cruise flight. A brief outline of results is given here. In Figure 20, a comparison of drag related quantities is given for a) fully turbulent conditions (top line), b) laminar-turbulent conditions with predicted transition

(indicated by pink line) without suction in the RANS calculation (center line) and c) laminar-turbulent

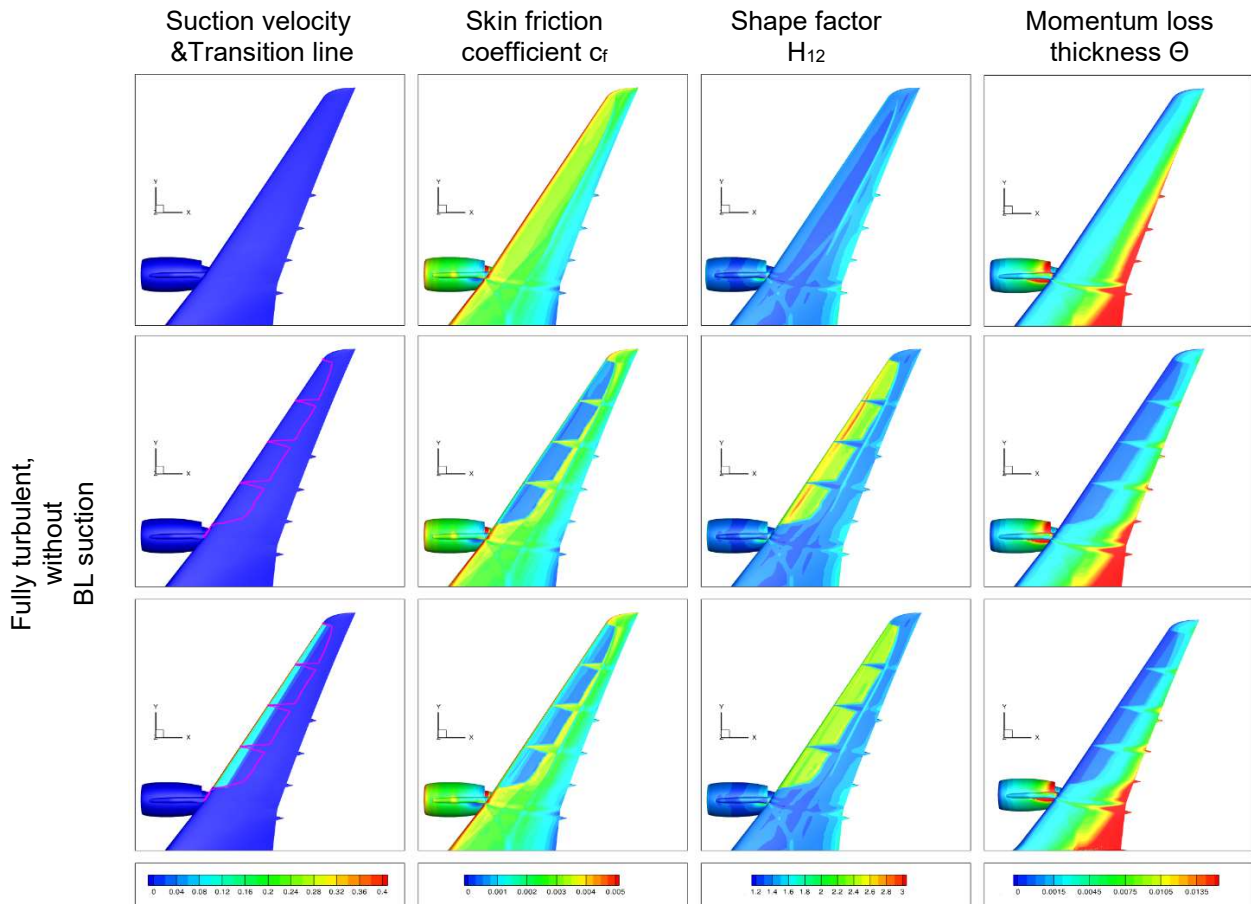


Figure 20 Impact of viscous wall boundary conditions on skin friction, shape factor and momentum loss thickness. GBD-DLR-2 Testcase, $c_L=0.5$, $M=0.83$, FL360.

conditions with predicted transition with active suction boundary condition (bottom line). The CQ distribution given in Figure 18, was used for all four HLFC suction panels of the configuration. For case b) suction is only considered in the context of transition prediction, employing an external boundary layer solver (see Figure 17). With regard to skin friction coefficient (center left row), a significant reduction is achieved when boundary conditions are changed from turbulent to free-transition conditions. If the suction boundary condition activated, a clear increase of c_f in the area of the suction panels is observed compared to the case with free transition and no suction. Nevertheless, in comparison with the fully turbulent case, the reduction in skin friction from laminarization by the HLFC system remains significant.

The impact of suction on the shape factor is shown in the center-right row of Figure 20. Values of H_{12} up to 3 (red contour color) are present in the calculation with free transition without suction. Here, the laminar flow is highly decelerated. When activating boundary layer suction, these high values of H_{12} disappear. The laminar boundary layer is stabilized and the tendency to flow separation is reduced. The influence of the different boundary conditions on momentum loss thickness θ is presented in the right row of Figure 20. The boundary layer in the laminar turbulent case without suction is clearly thinner than in the fully turbulent case. With active suction, the reduction of θ is slightly more pronounced.

An important observation is that the active suction has no significant influence on the calculated transition position in the cases shown. This is the case because the linear stability analysis is based on boundary layer data from an external boundary layer code and the pressure distribution does not

change significantly with boundary layer suction.

Overall, the 3D test case shows the same effects of boundary layer suction on boundary layer development as were previously observed for the infinite swept wing. With respect to performance prediction drag values are given in Table 2.

Boundary Conditions	Drag reduction compared to fully turbulent BC [%]
Free transition without suction in RANS	4.38
Free transition with active suction in RANS	4.01

Table 2: Drag reduction results for cases with and without active boundary layer suction in RANS simulations. Testcase GBD-DLR-2, $c_L=0.5$, $M=0.83$, $Re= 47.2E6$

The predicted drag savings of 4.38% using the (former state-of-the-art) method without boundary layer suction in the CFD solver are reduced to 4.01% when calculating with suction. This makes a difference of 8.5% in the predicted resistance savings. Therefore, the use of the new extraction boundary conditions in the TAU code is recommended for future HLFC projects where accurate performance prediction is critical. Using a lower suction rate is found to give less drag increase due to suction. This will be the case for the optimized suction distribution.

6.2 Adapted transition prediction considering technology effects

In view of the significant influence of the laminar region extent on aerodynamic performance assessment, an additional investigation was carried out aiming at providing a more realistic laminar region. This was performed by taking into account technology effects consistent with the HLFC systems designed within the HLFC-WIN project. Regarding laminar/turbulent transition, the suction magnitude was reduced without compromising the laminar region extent and the suction area was adjusted to the spanwise variation in the front spar location. Turbulent wedges were introduced at segment boundaries, where a 15° opening angle assumption was made. Finally, the transition line from stability analysis results in nine sections across all four HLFC segments was superimposed with the aforementioned turbulent wedges and lead to a more realistic laminar area extent. It should also be noted that this limits the inboard extent of the laminar region with respect to the previous free transition computations. Free transition computations are more optimistic in that aspect because they were performed before the exact definition of the panel extent in the finalized HLFC system. The laminar region modification in this updated transition computation can be seen in Figure 21, which shows a comparison of skin friction and the transition line for the two types of laminar/turbulent computations. Figure 22 shows a comparison of the transition line on the wing upper surface for the adapted transition computation described above and the laminar/turbulent computations analyzed in section 4.3. This comparison gives a clearer view of the laminar region reduction when considering a limited spanwise extent of the laminar region, as well as introducing turbulent wedges between segment boundaries. As also shown (in Figure 5), the geometry modifications introduced in the GBD-DLR-3 geometry are confirmed to have a minimal but beneficial effect on the extent of the laminar region, compared to the DLR-2.

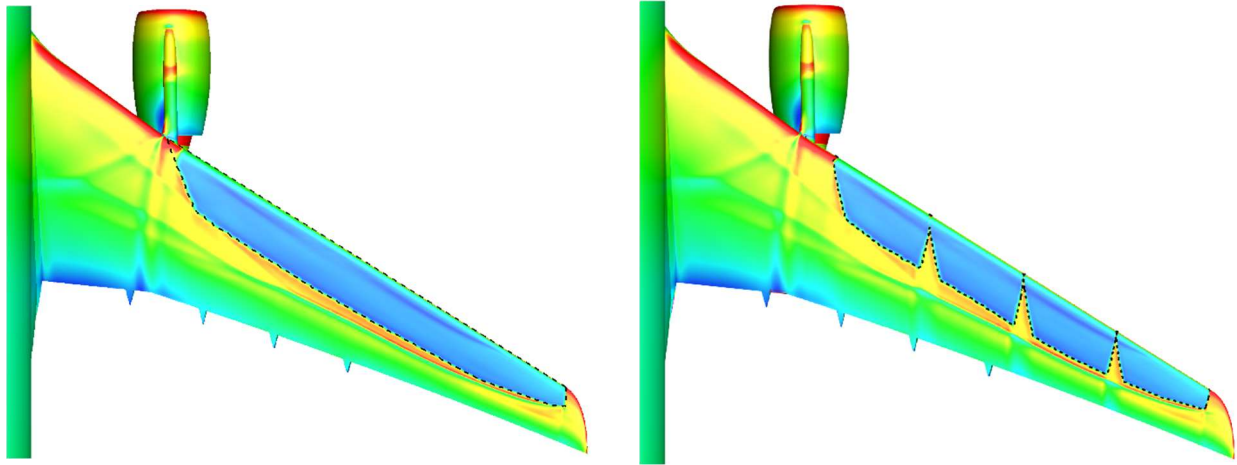


Figure 21 Magnitude of skin friction coefficient for the HLFC GBD-DLR-2 variant with free transition (left) and adapted transition (right).

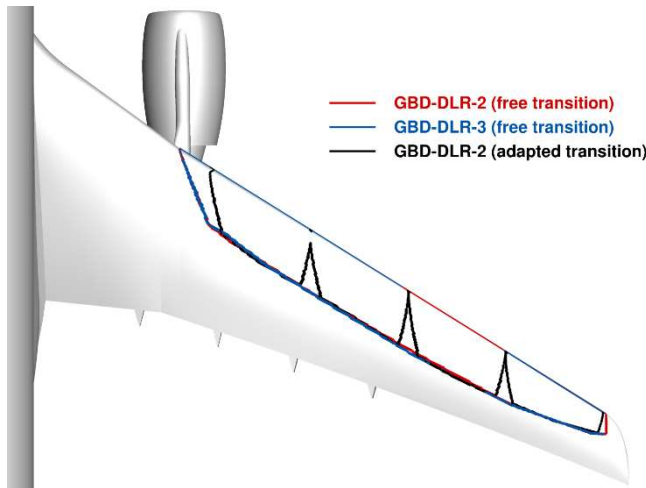


Figure 22 transition line comparison for the laminar/turbulent computations

The influence of the adapted transition prediction on the overall aerodynamic performance is summarized in Table 3. The reduced laminar region extent leads to increased viscous drag, and therefore to an increase of most near-field and far-field coefficients. Induced drag also shows a minor increase, whereas wave drag is slightly reduced with respect to the free transition laminar/turbulent computation. The overall penalty when considering a more realistic laminar region compared to the free transition case is shown to be reduction of the drag benefit by 0.29% with respect to the total far-field drag of the reference XRF-1 aircraft. In terms of spanwise distribution of drag components,

modifications due to the adaptation of the transition prediction, were found to be small, but consistent with the overall values presented in Table 3.

Geometry	Transition type	AoA (°)	ΔCD_p	ΔCD_f	ΔCD_{vp}	ΔCD_w	ΔCD_i	ΔCD_{sp}	ΔCD_{ff}	Laminar surface [%]
GBD-DLR-2	Free Transition	2.682	-1,13%	-4.69%	-16.92%	+85,29%	-0,20%	-10.17%	-2.86%	14.26%
	Adapted Transition	2.691	-0.94%	-4.50%	-16.32%	+81.84%	-0.13%	-13.56%	-2.57%	13.32 %

Table 3 Influence of a refined transition prediction on near-field and far-field drag coefficient increments (w.r.t. the reference XRF-1 aircraft) computed with the ffd72 software for the two HLFC geometries at cruise conditions. The laminar surface percentage is computed with respect to the wing surface, excluding the pylon and FTFs.

7. Conclusions

This paper presents the design and aerodynamic performance assessment of realistic HLFC wing configurations, designed by DLR within the Clean Sky 2 HLFC-WIN project. Aerodynamic performance has been assessed using the *ffd72* far-field drag analysis software of ONERA, based on fully turbulent and laminar/turbulent CFD computations at a cruise operating point including engines with power-on boundary conditions. The design involves wing shape design and for the suction panels the optimization of suction distribution and chambering design. Shape design has been performed using the DLR 3D inverse transonic design code. For the optimization of the suction distribution the DLR tool chain TASG has been used and for the suction panel chamber design the program SCDP by Schrauf.

Several HLFC wing geometries have been designed and analyzed. They were designed by DLR based on a HLFC variant of the XRF-1 research geometry, designed by Airbus. The HLFC region is restricted to the outer wing. For the shape design a generalized suction distribution is used for the suction panels. The first shape design, denoted GBD-DLR-2, provided the wing geometry for the large-scale ground-based demonstrator of the HLFC-WIN project. In comparison to the initial HLFC design it has a larger laminar extent and an increased airfoil thickness distribution. The second shape design is an improved version of this geometry aiming at improving its aerodynamic performance, considering results of the far-field drag analysis of the original version. Far-field drag analysis shows that HLFC designs introduce an important drag benefit. This laminarization benefit can be mainly attributed to the friction and viscous pressure drag components. A wave drag penalty, is also identified. The estimated benefit of the improved outer HLFC wing with respect to the original XRF-1 aircraft is estimated to be in the order of 3.71% at the cruise design point. This benefit is however slightly reduced (reduction in the order of 0.29% for the GBD-DLR-2 geometry) when considering an adapted transition approach, which takes into account technology integration effects (exact suction panel placement, and turbulent wedges between segments). In addition to these investigations aiming at evaluating cruise aerodynamic performance, additional design studies have been presented. A further shape design showed, that a NLF design is possible in the region of the outermost suction panel of the HLFC wing. Despite the large leading edge sweep and Reynolds numbers typical of a long-range aircraft, the design of a NLF region was possible by using crossflow attenuated NLF (CATNLF) design in the nose region. For the GBD-DLR-2 geometry a suction optimization and chamber design was performed considering different relevant cruise flow conditions along the transonic cruise flight. This was achieved via a novel approach combining variable porosity of outer skin and suction chambers.

In addition to the design and analysis of HLFC geometries, this work also describes extensions to the numerical methods used in this context. The introduced enhancements to the transition module of the TAU code now allow fully automatic, LST-based transition prediction also for HLFC configurations. Consideration of the boundary layer suction in the CFD solver via special boundary conditions improves the physical modeling and permits more accurate performance prediction. The improved methods have been successfully applied to an infinite swept wing and the GBD-DLR2 HLFC configuration

The results have shown that the DLR inverse design tool was appropriate to perform efficiently the transonic cruise shape design of the HLFC configuration. The HLFC shape design requires consideration of flow cases for different transonic cruise conditions. In contrast to NLF cases, this is necessary not only for obtaining a good aerodynamic performance but also for achieving low suction power. The results presented, highlight that an efficient shape design method, the physical insight and quantification of the influence of the different mechanisms behind drag reduction, a refined transition prediction as well as the use of numerical methods of adequate fidelity, are elements that will be of significant importance for the design and implementation of HLFC technology in future passenger aircraft.

8. Acknowledgment

This work was funded by the European Union within the frame of the HLFC-WIN project. This project is part of the Clean Sky 2 Joint Undertaking under the European Union's Horizon 2020 research and innovation programme (Grant agreements CS2-GAM-2018-LPA-AMD-807097-38 and CS2-GAM-2020-LPA-AMD-945583-11). The HLFC code development was funded by German Federal Ministry for Economic Affairs and Energy within the German Aeronautical Research Program LuFo V-3/2018-2022 In.Fly.Tec/Aplaus under grant agreement no 20A1705C.

9. Contact author email address

The contact author email address is: th.streit@dlr.de

10. Copyright Statement

The authors confirm that they, and/or their company or organization, hold copyright on all of the original material included in this paper. The authors also confirm that they have obtained permission, from the copyright holder of any third party material included in this paper, to publish it as part of their paper. The authors confirm that they give permission, or have obtained permission from the copyright holder of this paper, for the publication and distribution of this paper as part of the ICAS proceedings or as individual off-prints from the proceedings.

References

- [1] Advisory Council for Aviation Research and Innovation in Europe (ACARE), Strategic Research and Innovation Agenda (SRIA), <https://www.acare4europe.org/sria>, accessed on 22th April 2022.
- [2] A. Bauen, N. Bitossi, L. German, A. Harris and K. Leow, "Sustainable Aviation Fuels," *Johnson Matthey Technology Review* 64, (3), 263–278, 2020.
- [3] Seitz, A., Horstmann, K.H., Design studies on NLF and HLFC Applications at DLR, 27th International Congress on the Aeronautical Sciences, 19.-24. Sep., Nice, France, 2010.
- [4] Krishnan, K. S. G., Bertram, O., & Seibel, O. (2017). Review of hybrid laminar flow control systems. *Progress in Aerospace Sciences*, 93, 24-52.
- [5] Hue, D., Vermeersch, O., Bailly, D., Brunet, V., & Forte, M. (2015). Experimental and numerical methods for transition and drag predictions of laminar airfoils. *AIAA Journal*, 53(9), 2694-2712.
- [6] Hue, D., Vermeersch, O., Duchemin, J., Colin, O., & Tran, D. (2018). Wind-tunnel and CFD investigations focused on transition and performance predictions of laminar wings. *AIAA Journal*, 56(1), 132-145.
- [7] Streit, T., Wedler, S. and Kruse, M., "DLR natural and hybrid transonic laminar wing design incorporating new methodologies", *Aeronautical J*, 2015, **119**, (1221), pp 1303-1326.
- [8] Kroll, N., Abu-Zurayk, M., Dimitrov, D. *et al.* DLR project Digital-X: towards virtual aircraft design and flight testing based on high-fidelity methods. *CEAS Aeronautical Journal* 7, 3–27 (2016).
- [9] Carini, M., Blondeau, C., Fabbiane, N., Meheut, M., Abu-Zurayk, M., Feldwisch, J. M., Caslav, I. & Merle, A. (2021). Towards industrial aero-structural aircraft optimization via coupled-adjoint derivatives. In *AIAA Aviation 2021 Forum*, Paper 2021-3074.
- [10] D. Schwarmborn, T. Gerhold, R. Heinrich, "The DLR TAU-Code: Recent Applications in Research and Industry", *Proceedings of European Conference on Computational Fluid Dynamics ECCOMAS CFD 2006*, Delft, Netherlands.
- [11] Streit, T., Hoffrogge, C., DLR transonic inverse design code, extensions and modifications to increase versatility and robustness, *The Aeronautical Journal*, 2017, **121**, (1245), pp 1733-1757.
- [12] Kroll, N. and Fassbender, J.K. MEGAFLOW –Numerical Flow Simulation for Aircraft Design, *Notes on Numerical Fluid Mechanics and Multidisciplinary Design (NNFM)* vol. **89**, Springer Verlag, Closing Presentation DLR Project MEGAFLOW Braunschweig (de), 10–11 January 2002.
- [13] SOLAR 15.3.7 M Leatham, S Stokes, J A Shaw, J Cooper, J Appa, T A Blayloc. Automatic Mesh Generation for Rapid-Response Navier-Stokes Calculations, *AIAA Paper 2000-2247*, 2000.
- [14] Krimmelbein, N., Krummbein, A., Industrialization of the Automatic Transition Prediction in the DLR TAU Code, *Notes on Numerical Fluids Mechanics and Multidisciplinary Design*, book series (NNFM, volume 123), Computational Flight Testing, pp. 89-98, 2013.

- [15] Schrauf, G., LILO 2.1 – Users Guide and Tutorial, GSSC Technical Report, July 2006.
- [16] Schrauf, G., COCO – A Program to Compute Velocity and Temperature Profiles for Local and Nonlocal Stability Analysis of Compressible, Conical Boundary Layers with Suction, ZARM Technik Report, November 1998.
- [17] Kilian, T., Wedler, S., TASG - An integrated method for the aerodynamic design of HLFC systems. Deutscher Luft- und Raumfahrtkongress, 01.-02. Sep. 2020, Deutschland.
- [18] G. Schrauf, "SCDP - A Suction Chamber Design Program - Version 1.4, Technical Report, GSSC TR 8.4," Bremen, Germany, 2013.
- [19] Kilian, T., Horn, M., Verification of a chamberless HLFC design with an outer skin of variable porosity. CEAS Aeronautical Journal, Springer, 2021.
- [20] Van Der Vooren, J., and Destarac, D., "Drag/thrust analysis of jet-propelled transonic transport aircraft; definition of physical drag components," *Aerospace Science and Technology*, Vol. 8, No. 6, 2004, pp. 545–556.
- [21] Destarac, D., "Far-Field / Near-Field Drag Balance and Applications of Drag Extraction in CFD, In: CFD-based Aircraft Drag Prediction and Reduction", VKI Lecture Series 2003, Von Karman Institute for Fluid Dynamics, Rhode Saint Genèse, February 3-7, 2003, National Institute of Aerospace, Hampton (VA), November 3-7, 2003.
- [22] Bailly D., Petropoulos I., Wervaecke C., Méheut M., Atinault O. & Fournis C. (2021) An overview of ONERA research activities related to drag analysis and breakdown, AIAA Aviation Forum, AIAA Paper 2021-2551, Virtual Event.
- [23] Petropoulos I., Streit T., Kilian T., Kruse M. (2022), Numerical aerodynamic performance assessment of HLFC wing configurations using far-field drag analysis, 56th 3AF International Conference on Applied Aerodynamics (AERO2022), 28-30 March 2022, Toulouse, France.
- [24] Schrauf G., "Large Scale Laminar Flow Test Evaluated with Linear Stability Theory, Journal of Aircraft". Vol. 41, No. 2 ,2004.
- [25] Pfenninger, W., Laminar Flow Control. Laminarization. AGARD-R-654, (1977), pp.3-1-3-75.
- [26] Arnal D., Juillen J.C., Reneaux J., Gasparian G., Effect of Wall Suction on Leading Edge Contamination, *Aerospace Science and Technology*, vol. 8, pp 505-517, 1997.
- [27] Streit, T., Seitz, A., Hein, S., Kunze, P. (2020) NLF Potential of Laminar Transonic Long-range Aircraft. AIAA Aviation 2020 Forum, 15-19. June 2020, USA Virtual Event, doi: 10.2514/6.2020-2748.
- [28] Campbell, R. L. and Lynde, M. N., "Natural Laminar Flow Design for Wings with Moderate Sweep", 34th AIAA Applied Aerodynamic Conference, AIAA AVIATION Forum, AIAA 2016-4326, June 2016., <https://doi.org/10.2514/6.2016-4326>.
- [29] Lynde, M. N. and Campbell, R., "Computational Design and Analysis of a Transonic Natural Laminar Flow Wing for a Wind Tunnel Model", AIAA 2017-3058, June 2017.
- [30] J. Preist, B. Paluch, Design specifications and inspection of perforated panels for HLF suction systems. 2nd European Forum on laminar Flow technology, Bordeaux (France), June 10-12, 1996.
- [31] D. G. MacManus, An Aerodynamic Prediction Technique for Laminar Flow Control Suction Surfaces. Dissertation., Department of Mechanical Engineering, University College Galway, 1996.
- [32] Boeing Commercial Aircraft Group, High Reynolds Number Hybrid Laminar Flow Control (HLFC) Flight Experiment. Report 2; Aerodynamic Design, NASA/CR-1999-209324, 1999.
- [33] Krimmelbein, N. and Krumbein A., "Automatic Transition Prediction for Three-Dimensional Configurations with Focus on Industrial Application", AIAA 2010-4292, 40th Fluid Dynamics Conference and Exhibit, Chicago, Illinois. <https://doi.org/10.2514/6.2010-4292>.
- [34] Schrauf, G. and Frhr von Geyr, H., "Simplified hybrid laminar flow control for transport aircraft", Ecomas European Congress on Comp. Methods in Applied Sciences and Engineering, 2012.
- [35] Krimmelbein, N. and Krumbein, A. "Transition prediction for flows with suction using the eN-method," AIAA 2021-0630. AIAA Scitech 2021 Forum, 2021. <https://doi.org/10.2514/6.2021-0630>.